The role of slow screw dislocations in controlling fast strain avalanche dynamics in body-centered cubic metals

Article *in* International Journal of Plasticity · August 2019

DOI: 10.1016/j.ijplas.2019.08.008

CITATIONS
4

READS
372

6 authors, including:

Yinan Cui
Tsinghua University
34 PUBLICATIONS **406** CITATIONS
SEE PROFILE

Giacomo Po
University of Miami
70 PUBLICATIONS **681** CITATIONS
SEE PROFILE

Pratyush Srivastava
University of California, Los Angeles
2 PUBLICATIONS **4** CITATIONS
SEE PROFILE

Vijay Gupta
University of California, Los Angeles
83 PUBLICATIONS **1,276** CITATIONS
SEE PROFILE

The role of slow screw dislocations in controlling fast strain avalanche dynamics in body-centered cubic metals

Yinan Cui[a,b], Giacomo Po[b,c], Pratyush Srivastava[b], Katherine Jiang[d], Vijay Gupta[b], Nasr Ghoniem[b]

[a]*Applied Mechanics Lab., School of Aerospace Engineering, Tsinghua University, Beijing 100084 China*
[b]*Department of Mechanical and Aerospace Engineering, University of California Los Angeles, Los Angeles, CA 90095*
[c]*Department of Mechanical and Aerospace Engineering, University of Miami, Coral Gables, FL 33146*
[d]*Department of Material Science and Engineering, University of California Los Angeles, Los Angeles, CA 90095*

Abstract

Plasticity in body centered cubic (BCC) crystals is shown to be controlled by slow screw dislocation motion, owing to the thermally-activated process of kink pair nucleation and migration. Through three dimensional discrete dislocation dynamics simulations, this work unravels the mystery of how such slow screw dislocation behavior contributes to extremely rapid strain bursts in submicron BCC tungsten (W) pillars, which is typical of BCC metals. It is found that strain bursts are dominated by the motion of non-screw dislocations at low strain rate, but are more influenced by screw dislocations at high strain rate. The total, and partial strain burst magnitude due to screw dislocations alone, are found to exhibit rate dependence following a power law statistics with exponent of 0.65. Similar power law statistics are also obeyed for the standard deviation of the corresponding plastic strain rate. The role of screw dislocations is attributed to the changing nature of dislocation source operation at different strain rates. The corresponding spatial distribution of plastic deformation is also discussed based on the uniqueness of the simulation method in reproducing the distribution of slipped area and plastic strain with very high spatial resolution.

Keywords: Screw dislocation, BCC crystal, strain burst, statistics, dislocation mechanism

Contents

Email address: cyn@mail.tsinghua.edu.cn (Yinan Cui)

1. Introduction

Avalanches phenomena are very commonly observed in many physical systems, for example in earthquakes, rocks, and granular materials (Uhl et al., 2015). These phenomena have attracted considerable attention because of the universality of behavior regardless of the underlying mechanisms, and because such universality is intimately related to critical phenomena in non-equilibrium physical systems. In recent years, dislocation avalanches and strain bursts are widely found during plastic flow, particularly at the nano- and micro-scales (Brechtl et al., 2019; Maaß and Derlet, 2018; Ni et al., 2017; Papanikolaou et al., 2017; Song et al., 2019a; Wang et al., 2018; Zaiser, 2006). From a fundamental viewpoint, dislocation avalanche statistics is analogous to other nonequilibrium physical systems of vastly different spatial and temporal scales, implying the universality of underlying physics. In addition, such intermittent plastic flow in small-scale materials is a paradigm shift from traditional well-defined continuous and deterministic behavior (Krebs et al., 2017; Salmenjoki et al., 2018; Zhang et al., 2016). This challenges the effective description of deformation kinetics, and the applicability of conventional crystal plasticity models to micro- and nano-scale crystals. Moreover, from an engineering standpoint, controllability of plastic flow during the manufacturing and operation of micro-devices can become very challenging.

During crystal deformation, strain bursts enabled by dislocation avalanches generally correspond to the condition that the internal plastic strain rate $\dot{\varepsilon}^p$ is higher than the applied strain rate $\dot{\varepsilon}_a$. This is manifest as a stress drop signal (stress relaxation) in stress-strain curves during strain control loading mode. On the other hand, during stress control loading mode, strain bursts are manifest as stress steps of varying amounts of plastic strain accumulated in each step (see Fig. S2 in (Cui et al., 2016a) and Fig. 1 in (Maaß et al., 2015) as examples). According to Orowan's law, the internal plastic strain rate $\dot{\varepsilon}^p$ is the product of the mobile dislocation density ρ, Burgers vector magnitude b, and the dislocation velocity v (i.e. $\dot{\varepsilon}^p = \rho b v$). Therefore, high strain rates $\dot{\varepsilon}^p$ required for the occurrence of strain bursts are expected to be accompanied with high dislocation velocity. Namely, the collective and rapid dislocation motion is the origin of the strain burst (Csikor et al., 2007). This raises several intriguing questions: (1) The plastic behavior in body centered cubic (BCC) crystals is widely believed to be controlled by the motion of screw dislocations (Cereceda et al., 2016; Kaufmann et al., 2013; Lim et al., 2015; Po et al., 2016), whose velocity is much lower than that of edge dislocations. If we set the average velocity of the screw dislocations and edge dislocations under the same resolved shear stress as a reference value, in BCC the screw dislocation velocity will be much lower than the reference velocity. Therefore, in the following discussions, we sometimes use the description of "slow screw dislocation motion". This is a direct result of the thermally-activated process of kink pair nucleation and migration with a high Peierls energy barrier. How can then the slow motion of screw dislocations cause very rapid strain bursts? If one finds out why, then the next question would be regarding the special role of screw dislocations in initiating and controlling intermittent plasticity? (2) The occurrence of a strain burst depends on the competition between internal dislocation dynamics and the external loading rate (Cao and Koslowski, 2015; Song et al., 2019b; Sparks and Maaß, 2018a; Zhao et al., 2018). Then, how do screw dislocations contribute to triggering strain bursts when the applied strain rate is relatively high? (3) The plastic strain rate is also sensitive to the temperature. In addition to tuning external temperature, the dissipated energy due to plastic deformation also contributes to increasing the local temperature (Le et al., 2017). The change in temperature on the one hand influences the dislocation mobility, and on the other hand affects the kinetics of thermally activated dislocation depinning. The latter aspect is theoretically described in (Langer, 2006; Langer and Pechenik, 2003; Langer et al., 2010; Le et al., 2017) within a thermodynamic framework. Generally, a higher temperature leads to faster dislocation motion, faster dislocation depinning and larger plastic strain rate. (4) In submicron face centered cubic (FCC) crystals, the one-to-one correspondence between the strain burst and the operation of a single arm source is revealed (Cui et al., 2014, 2016a; Kiener and Minor, 2011; Rao et al., 2008). In BCC crystals, however, since slow screw dislocations lead to new features of dislocation source operation (Cui et al., 2016b; Yu et al., 2019; Zhang et al., 2017), one would be interested to know whether similar single arm source mechanisms still control the burst behavior?

Most of the previous work has focused on the statistical characterization of strain bursts in BCC crystals. The strain burst magnitudes have been found to follow a power law distribution in stress-controlled compressive deformation of monocrystalline molybdenum micropillars (Brinckmann et al., 2008; Zaiser et al., 2008). Recent experiments on BCC Nb pillar shows that the power law exponent varies with the change of the applied strain rate (Sparks and Maaß, 2018a). With respect to the strain burst mechanism in BCC, the majority of prior efforts have been employed to study the pop-in behavior during nanoindentation tests (Kositski and Mordehai, 2015; Vadalakonda et al., 2006; Wang and

Ngan, 2004). In this case, the dislocations are strongly pinned beneath the indenter, the strain burst is found to be associated with the interaction between the depinned dislocation and pinned dislocations (Kositski and Mordehai, 2015). Till now, a clear connection between intermittent plasticity and screw dislocation behavior in BCC crystals is yet to be revealed (Lehtinen et al., 2016). With current experimental techniques, rapid dynamic dislocation behavior during burst event is difficult to be fully captured by in-situ experiments. It is also very difficult or even impossible to fully distinguish the contribution of screw dislocations alone. On the other hand, three dimensional discrete dislocation dynamics (3D-DDD) computer simulations can be an effective tool to capture underlying dislocation mechanisms (Huang et al., 2014; Jamond et al., 2016; Liu et al., 2017; Sills et al., 2018). Through incorporating an atomistic-informed dislocation mobility law in BCC materials (Po et al., 2016), the possibility of revealing the mysterious role of screw dislocations during strain bursts becomes real.

In the present work, tungsten (W) is chosen as an example of a BCC crystal, due to its extensive application in high-temperature and plasma-facing components. The 3D-DDD simulation method is mainly employed in the study. Improvements of our original 3D-DDD method that enable accurate strain calculations are first described in section 2. Simulation results are then compared with corresponding experimental data to validate the calculations. The strain burst behavior at room temperature at different strain rates is discussed in section 3. The role of screw dislocations is then revealed in section 4. Finally, concluding remarks are given in section 5.

2. Simulation Methodology & Experimental Validation

The investigative tool employed here is the MoDELib (Mechanics of Defect Evolution Library) computer code (Po and Ghoniem, 2015), described in detail in our previous publications (Ghoniem et al., 2000; Po et al., 2014). In this 3D-DDD computer simulation approach, curved dislocation lines are discretized into a succession of parameterized segments. Configurational Peach-Koehler forces are then computed, and a system of equations for the motion of nodes connecting these segments is solved in a way similar to the traditional finite element method (FEM), as described in detail in (Cui et al., 2018b; Po et al., 2014). Boundary conditions and image forces are considered by coupling the infinite medium results with an FEM solution of an elasticity problem using the superposition principle (Po et al., 2014). When using the superposition method, the interaction stress between dislocations is mainly obtained based on the analytical solution of dislocation stress field. When uniaxial loading is applied, the heterogeneity of the calculated stress by FEM is mainly induced by the image force, which is more important in the near surface region. Therefore, the calculated distribution of stress is relatively uniform, and there is no need to use very fine meshes. We used 2653 second-order tetrahedra elements in the current calculations, and found that decreasing the mesh size had a small influence on the results.

The dislocation mobility law of BCC W is described in detail in our reference (Po et al., 2016). Since dislocation mobility is significantly different for screw and edge dislocations, the velocity v_m of an arbitrary mixed dislocation segment is calculated by separating the edge and screw components, and the total velocity is written as,

$$v_m = v_e \cdot w(\theta) + v_s \cdot (1 - w(\theta)) \tag{1}$$

where θ is the angle between the dislocation tangent direction and the Burgers vector direction. $w(\theta)$ is dimensionless weigh function with properties $\lim_{\theta\to 0} w(\theta) = 0$, and $\lim_{\theta\to \pi/2} w(\theta) = 1$. Here, $w(\theta)$ is taken as $sin^2\theta$ (Po et al., 2016).

For screw dislocations, kink nucleation and motion are considered through an Arrhenius-type equation of the form,

$$v_s(\boldsymbol{\sigma}, T) = \begin{cases} \frac{\tau b}{B(\boldsymbol{\sigma},T)} \exp\left(-\frac{\Delta G_{kp}(\boldsymbol{\sigma},T)}{2k_B T}\right) & \text{if } \Delta G_{kp}(\boldsymbol{\sigma}, T) > 0 \\ \frac{\tau b}{B(\boldsymbol{\sigma},T)} & \text{if } \Delta G_{kp}(\boldsymbol{\sigma}, T) \leq 0 \end{cases} \tag{2}$$

where τ is the resolved shear stress. $B(\sigma, T)$ is the drag coefficient, which is a function of stress σ and temperature T, as given in Eq. (36) in (Po et al., 2016). The Gibbs free energy for kink pair nucleation, ΔG_{kp}, is given by the phenomenological relations, as given in Eq. (25) in (Po et al., 2016). The calculation of ΔG_{kp} considers the non-Schmid effects, the tension-compression asymmetry and the twinning-anti twinning asymmetry of BCC crystals. The velocity of the edge component, v_e, is determined by the total force acting on it divided by the viscous drag coefficient.

$$v_e = \frac{\tau b}{B(\sigma, T)} \tag{3}$$

The related parameters used in the mobility law are listed in Table 1 and Table 2 in (Po et al., 2016). Similar to the idea proposed in Srivastava et al. (2013), the screw dislocation has the highest kink-pair nucleation probability with the lowest Gibbs free energy. Therefore, if $\Delta G_{kp} > 0$, cross-slip automatically occurs by firstly comparing the Gibbs free energy corresponding to all the possible glide planes and then selecting the glide plane as the one with the lowest ΔG_{kp}. Otherwise, when $\Delta G_{kp} \leq 0$, cross slip occurs when the resolved shear stress on other possible glide planes is higher than that on the original glide plane.

Strain burst event physics is described in detail in (Cui et al., 2016a, 2017; Fressengeas et al., 2009; Weiss et al., 2007). We recall here only the main ideas. Considering that the plastic stain rate $\dot{\varepsilon}^p$ is a good measure of plastic deformation, it will be used here as a criterion parameter. A single avalanche/burst event is realized if the magnitude of the signal in a time series is greater than a threshold plastic strain rate $\dot{\varepsilon}^p_{\text{thr}}$,

$$\begin{aligned} \dot{\varepsilon}^p(t_s) = \dot{\varepsilon}^p(t_e) = \dot{\varepsilon}^p_{\text{thr}}, \\ \dot{\varepsilon}^p(t) > \dot{\varepsilon}^p_{\text{thr}} \quad \text{for } t_s < t < t_e \end{aligned} \tag{4}$$

where $\dot{\varepsilon}^p_{\text{thr}}$ is set to the applied strain rate. Two time constants, t_s and t_e, represent the start and end times of a burst event. The accurate calculation of $\dot{\varepsilon}^p$ is therefore very important so as to effectively recognize a strain burst event. In order to decrease the numerical noise of calculating $\dot{\varepsilon}^p$, we recently developed a new technique. In most of the previous work, $\dot{\varepsilon}^p$ is calculated by summing the plastic strain rate induced by each dislocation segment based on their instantaneous velocity $\boldsymbol{v}$,

$$\dot{\varepsilon}^p = \frac{1}{\Omega} \sum_{i=1}^{N_{dis}} (\boldsymbol{b}_i \otimes \boldsymbol{v}_i + \boldsymbol{v}_i \otimes \boldsymbol{b}_i) \mathrm{d}l. \tag{5}$$

where N_{dis} is the total number of the dislocation segments, $\boldsymbol{b}_i$ and $\boldsymbol{v}_i$ are the Burgers vector and the velocity vector of the ith dislocation segment, Ω is the characteristic volume. In an actual calculation, the instantaneous dislocation velocity $\boldsymbol{v}$ can be influenced by numerical noise. For example, it is sometimes observed that small oscillations of dislocation segments around stable positions occur during numerical integration. In addition, it is difficult to accurately consider the effect of topology change (such as dislocation junction formation) in Eq. (5). When the applied strain rate is very low, such numerical noise plays a more important role because it may be even comparable to the applied strain rate. In addition, and during the course of long simulations, the gradual accumulation of numerical noise may exacerbate the situation. Therefore, we propose that $\dot{\varepsilon}^p$ is calculated through taking the time derivative of the plastic strain. Furthermore, the plastic strain itself must be very accurately calculated on the basis of the slipped area of moving dislocations, i.e.

$$\dot{\varepsilon}^p = \frac{1}{\Omega \mathrm{d}t} \sum_{j=1}^{N_{loop}} (\boldsymbol{b}_j \otimes \mathrm{d}\boldsymbol{A}_j + \mathrm{d}\boldsymbol{A}_j \otimes \boldsymbol{b}_j). \tag{6}$$

where N_{loop} is the total number of the dislocation loops (note that the summation is over individual loops, and that segments by themselves are not relevant). $\mathrm{d}\boldsymbol{A}_j$ is the area increment of the jth loop during time increment $\mathrm{d}t$. In the previous DDD-FEM (finite element method) coupling method based on the idea of eigen-strain, the plastic strain is also calculated from the slipped area (Cui et al., 2015; Lemarchand et al., 2001; Vattré et al., 2014). However, the spatial resolution of the plastic strain and the displacement in these methods depend on the FEM mesh size, because the plastic strain information is only recorded by localizing the discrete plastic strains to continuum material points. Even though the integration points can be arbitrarily positioned, and one can record the plastic strain distribution on these integration points during the calculation. One generally cannot predict the distribution of the plastic strain, so it is difficult to have the optimized initial position of the integration points a priori. If a very fine mesh is used for the whole model at each step, extensive computing time is required. To solve this problem, in the new version of our simulation method, we retain the dislocation loop as well as the segment/node features (i.e. duality of representation, see Appendix A for more details). This leads to a new possibility of accurately reproducing the slip area, calculating the displacement field at any point of interest [1] without interpolation, and determining the spatial distribution of

[1] Without knowing the slipped area, one cannot accurately calculate the displacement field from the current position of dislocation segments alone, due to the ambiguous determination of the solid angle contribution in Eq. 3.7 in (Ghoniem and Sun, 1999)

plastic strain (more discussions will be given in section 4.2) with arbitrarily high spatial resolution. One can also easily estimate the instantaneous localization extent of the plastic strain according to the slipped area enclosed by the dislocation loops, and decide the points and time steps of interest to calculate the local plastic stain. The accumulation of numerical noise of calculating plastic strain is also avoided. More details of these new features of the simulation method and its advantages will be presented in a subsequent dedicated paper.

In order to make a distinct between the respective contributions of screw and non-screw dislocation, the plastic strain rate induced by screw dislocations $\dot{\varepsilon}^p_s$ and the plastic strain rate induced by non-screw dislocations $\dot{\varepsilon}^p_{ns}$ are calculated as follows,

$$\begin{aligned} \dot{\varepsilon}^p_s &= \sum_{i=1}^{N_{dis}} \dot{\varepsilon}^p_{(i)} \cdot cos^2\theta_{(i)} \\ \dot{\varepsilon}^p_{ns} &= \sum_{i=1}^{N_{dis}} \dot{\varepsilon}^p_{(i)} \cdot sin^2\theta_{(i)} \end{aligned} \tag{7}$$

where the subscript (i) on the right hand side of the equation corresponds to the ith dislocation segment. More explanation of Eq. (7) is given in Appendix B. Such decomposition of the contribution of the screw and non-screw dislocation is consistent with Eq. (1).

Using the method described above, computer simulation of W micro-pillar compression along the [001]-orientation was carried out at room temperature. The considered diameters of the W pillar were 500 nm and 2000 nm, with diameter-to-height ratio of 3. The initial dislocation structure was produced by the relaxation of randomly created dislocation loops and single arm sources. The external strain rate used in the simulations ranged from $10s^{-1}$ to 10^3s^{-1}. 10 simulations were carried out for each strain rate for pillars with diameter 500nm, and more than 3 simulations were carried out for each strain rate for pillar with diameter 2000nm.

To validate the simulation results, corresponding experiments were also carried out on W-pillars. They were prepared using Focused-Ion Beam method from a polished (100) W single crystal sample (9mm diameter and 10 mm thick). The same sample diameter, diameter-to-height ratio, and loading orientation were considered in these experiments. The nano-compression tests were performed in-situ using the Hysitron PI 85L SEM PicoIndenter. Each pillar was compressed using displacement control input to achieve the strain rates range of $10^{-3}s^{-1}$ to $10^{-1}s^{-1}$. More details on the experimental setup were given in our reference (Srivastava et al., 2019).

Fig. 1 shows a comparison of the experimental yield stress (0.2% offset), and the results of computer simulations. Fig. 1 demonstrates that the simulations are in reasonable agreement with the experiments. When the sample size is as large as 2000 nm, the well-known strain rate sensitivity of BCC crystals is captured, as indicated by the purple dash-dotted line. Namely, the higher the strain rate, the higher the flow stress. To compare with the results of bulk W, experimental results of references (Chen and Gray III, 1995; Dümmer et al., 1998) are also plotted in Fig. 1. The figure shows that the strain rate sensitivity of bulk samples is consistent with that in of the 2000 nm-diameter W pillars. In contrast, for samples with 500 nm diameter, the strain rate sensitivity is weaker, especially when the strain rate is lower than 10 s^{-1}. As the applied strain rate is decreased for small W pillars, the yield stress exhibits a transition from strain rate effect dominated to size-dominated behavior. These flow stress results will be analyzed more completely in a forthcoming publication (Srivastava et al., 2019). In the following, the strain burst behavior will be discussed mainly based on simulation results, with the added benefit of separating out the contribution of screw dislocations.

3. Influence of Strain Rate on Burst Statistics

The stress-strain curves, together with the evolution of the plastic strain rate obtained by simulations are presented in Fig. 2 (a-c) to illustrate the burst behavior of W pillars with 500 nm diameter under different applied strain rates. Here, we can define a 'normalized plastic strain rate', which is the plastic strain rate divided by the applied strain rate. For all considered cases, one can see that each significant peak of the normalized plastic strain rate corresponds to a strain burst event, which is manifest as the serrated feature of stress-strain curves. This is consistent with the definition given in Eq. (4). At lower strain rates, the normalized plastic strain rate fluctuates with a larger magnitude and higher

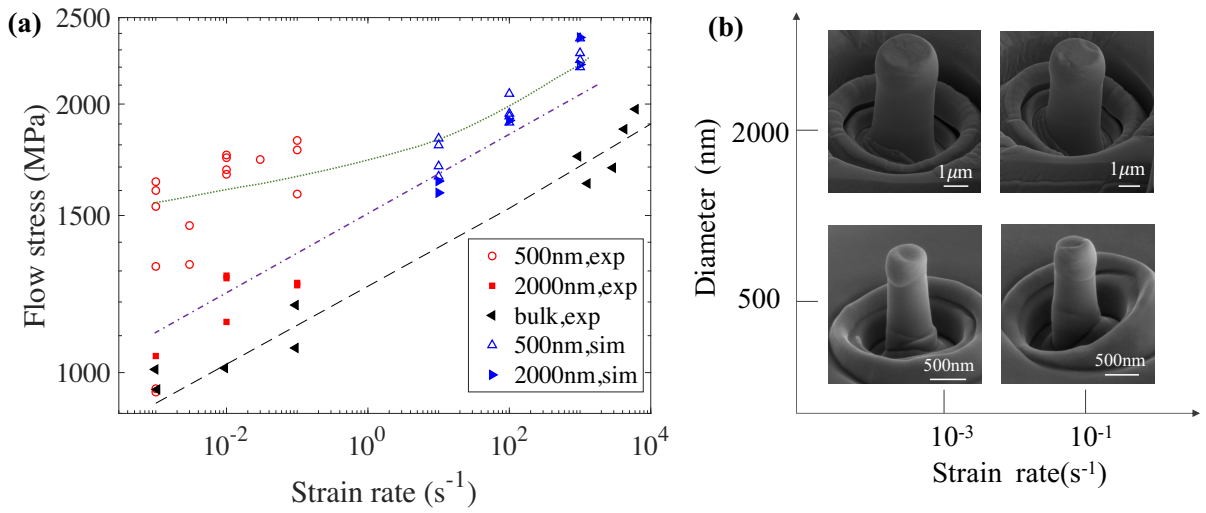

Figure 1: (a) Yield stress for a compressed W pillar with diameter 500 nm and 2000 nm obtained by experiments (Srivastava et al., 2019) (marked as 'exp' in the figure) and simulations (marked as 'sim' in the figure) under different strain rates $\dot{\varepsilon}_a$. The experimental data for bulk W are obtained from (Chen and Gray III, 1995; Dümmer et al., 1998). The Green dotted line, the purple dash-dot line, and the black dashed lines are plotted to show the yield stress trend as a function of applied strain rate for 500 nm-diameter, 2000 nm-diameter, and bulk W, respectively. The purple dash-dot line and the black dashed lines are proportional to $\dot{\varepsilon}_a^{0.055}$. (b) Scanning electron microscope (SEM) images of deformed W pillars. The corresponding strain value ε is 0.2 ± 0.02.

frequency. That is to say, when the applied strain rate is lower, it is easier and more frequent for the collective dislocation dynamics to reach much higher normalized plastic strain rate. A similar feature of the normalized plastic strain rate is also observed in the 2000 nm-diameter W pillar. This suggests that the burst frequency exhibits a strain rate dependence, which is consistent with recent experimental results by Sparks et al. (2019) on BCC Nb pillars.

Statistical analysis of the burst magnitude is further performed for 500 nm-diameter and 2000 nm-diameter W pillars, as given in Fig. 3 and Fig. 4. CCDF refers to the Complementary Cumulative Distribution Function. The reason for using CCDF instead of the probability distribution function is discussed in (Cui et al., 2017). The filled circle points correspond to the actual burst events distinguished through Eq. (4) using the total plastic strain rate $\dot{\varepsilon}^p$ as the criterion parameter. After determining the starting time t_s and the ending time t_e of one burst event according to Eq. (4), the burst displacement ΔU is equal to the displacement value at t_e minus the displacement at t_s. The burst duration Δt_d is calculated as $t_e - t_s$. Fig. 3 and Fig. 4 show that for a given probability, the burst displacement ΔU is smaller and the burst duration Δt_d is longer at lower strain rates. This trend can be understood from the evolution curve of the plastic strain rate in Fig. 2 (a-c). Note that the data number for the case of 2000nm and $1000 s^{-1}$ may not be sufficient to reflect the complete statistical behavior, but they can be used to reflect the trend.

Before analyzing the role of screw dislocations, one wonders whether the strain rate effect on burst statistics can be described in a more general way? Whether these burst displacement statistical curves can collapse into one curve for all these considered cases? We find that if we plot the $\Delta\varepsilon/\dot{\varepsilon}_a^{0.65}$, the CCDF of this burst quantity collapses for all considered cases, as shown in Fig. 5. Here, $\Delta\varepsilon$ is equal to the burst displacement normalized by the pillar height, and represents the burst strain. Fig. 5 (a) demonstrates that the burst strain has a nice scaling law with $\dot{\varepsilon}_a^{0.65}$. According to Eq. (4) and Fig. 2, a burst event is associated with the evolution of the plastic strain rate. A natural question is whether the strain rate dependent scaling law for burst strain shown in Fig. 5 is also manifest in some form in the evolution of the plastic strain rate? To answer this question, we calculate the average value and the standard deviation of the total plastic strain rate $\dot{\varepsilon}^p$. It is interesting to see that the standard deviation of the plastic strain rate during plastic deformation stage ($\varepsilon^p > 0.1\%$) also exhibits power law scaling relation with respect to the applied strain rate. Its exponent is also close to 0.65, as shown in Fig. 6 (b). Moreover, the average value of the plastic strain rate is close to applied strain rate. This is consistent with Fig. 2, where there is almost neither overall strain hardening nor softening. The analysis above clearly shows the statistical connection between burst quantity and plastic strain rate.

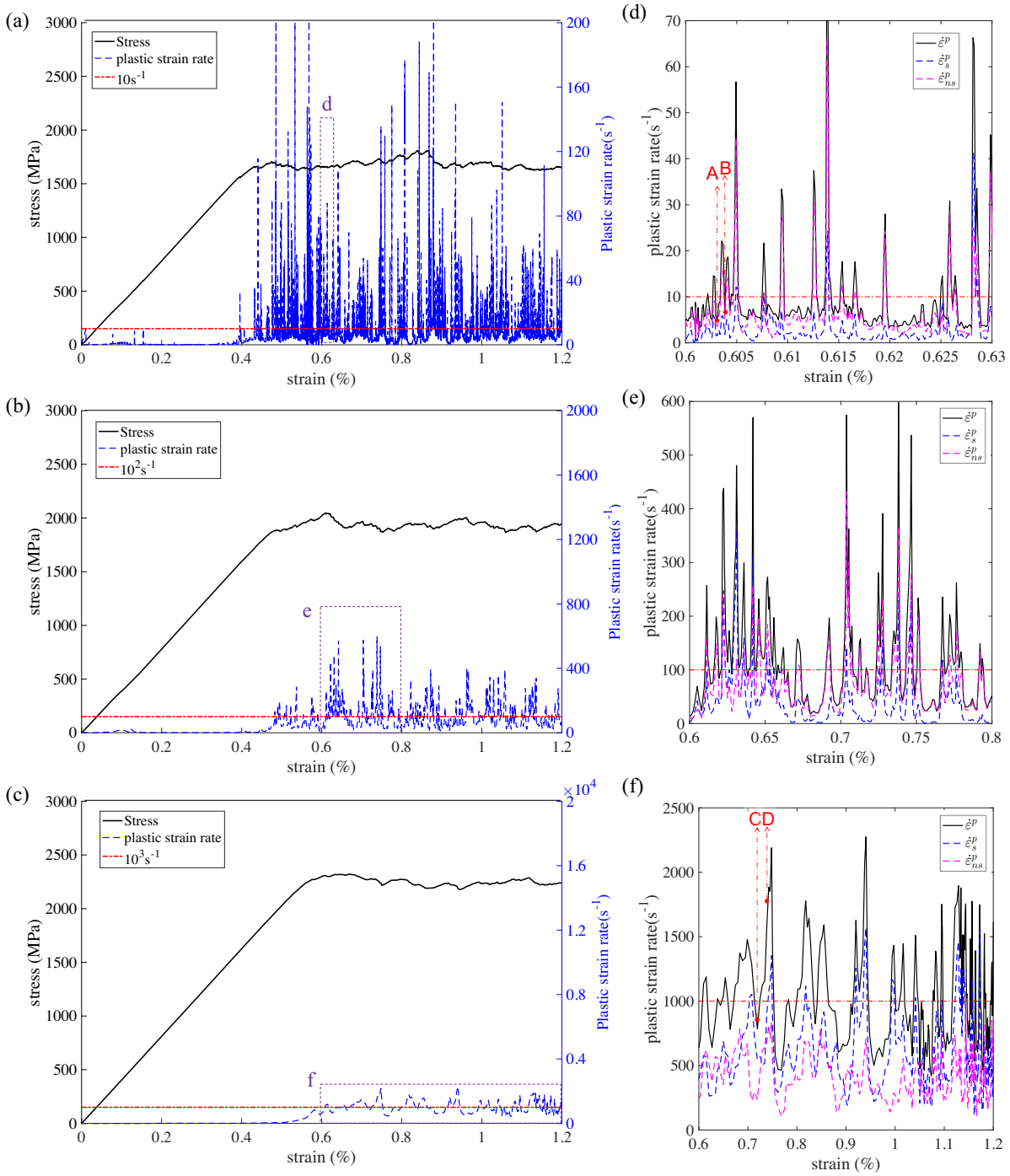

Figure 2: Evolution of the stress and plastic strain rate during deformation in a compressed W pillar with diameter 500 nm at strain rate (a) 10 s^{-1}, (b) 100 s^{-1}, (c) 1000 s^{-1}. (e-f) Higher magnification plot of the plastic strain rate evolution as marked in (a-c). $\dot{\varepsilon}^p$, $\dot{\varepsilon}^p_s$, $\dot{\varepsilon}^p_{ns}$ refer to the plastic strain rate induced by all dislocations, screw dislocations, and non-screw dislocations, respectively.

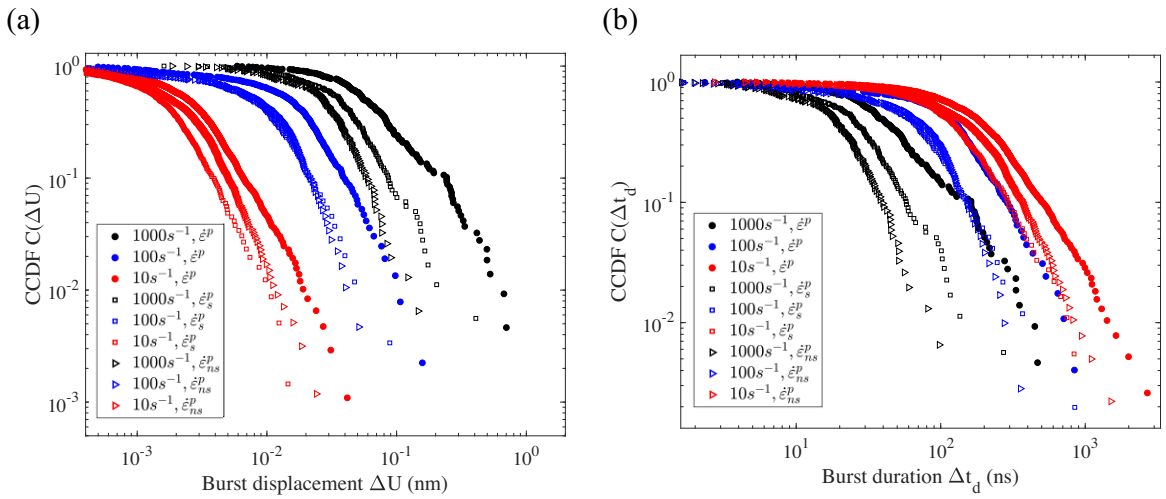

Figure 3: Statistical analysis of the burst size in compressed W pillar with diameter 500 nm, (a) burst displacement (ΔU), (b) burst duration. The filled circles correspond to the actual burst events distinguished by Eq. (4) using the total plastic strain rate $\dot{\varepsilon}^p$ as the criterion parameter, the hollow square points describe the virtual burst events if the plastic strain rate $\dot{\varepsilon}^p_s$ induced by pure screw dislocations is used in Eq. (4), while the hollow triangle points correspond to the plastic strain rate $\dot{\varepsilon}^p_{ns}$ induced by non-screw dislocations.

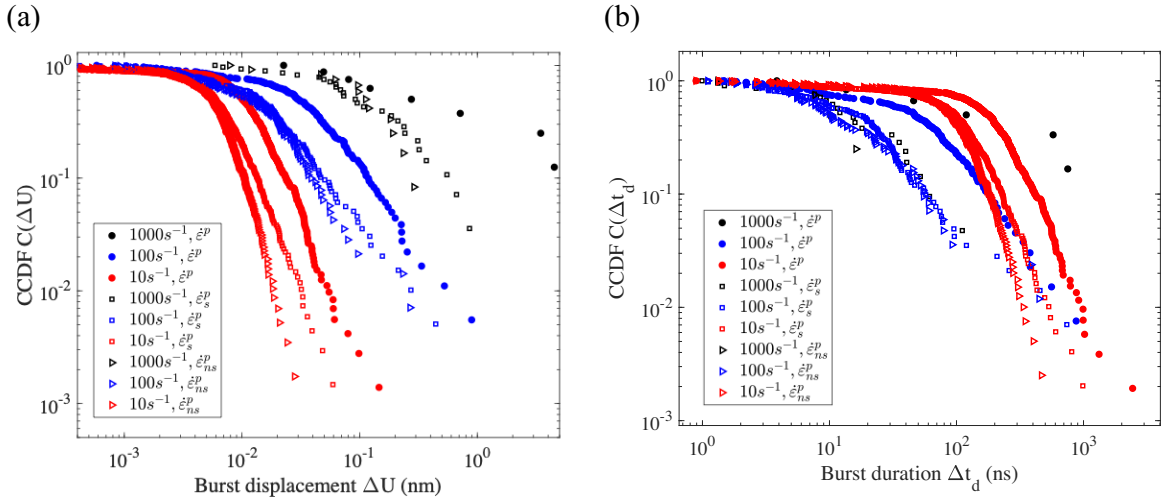

Figure 4: Statistical analysis of the burst size in compressed W pillar with diameter 2000 nm, (a) burst displacement, (b) burst duration. Explanation of the points is the same as that in Fig. 3.

4. Effects of Slow Screw Dislocation Motion

4.1. Screw Dislocation Contribution to Burst Statistics

In order to further distinguish the contribution of screw dislocations, we calculate "virtual" burst events through Eq. (4) by using the plastic strain rate $\dot{\varepsilon}^p_s$ due to screw dislocations alone, and the plastic strain rate $\dot{\varepsilon}^p_{ns}$ due to non-screw dislocations, respectively. Here, the threshold strain rate is also set to the applied strain rate. Therefore, the "virtual" burst events discerned using $\dot{\varepsilon}^p_s$ correspond to the burst event that can be triggered by screw dislocation alone, irrespective of the magnitude of $\dot{\varepsilon}^p_{ns}$. Examples of the evolution of $\dot{\varepsilon}^p_s$ and $\dot{\varepsilon}^p_{ns}$ are shown in Fig. 2 (d-f) and compared with the applied strain rate (red dash dotted line). The statistical properties of these virtual burst events are presented in Fig. 3 and Fig. 4. They can directly be used to discuss the relative role of screw and non-screw dislocations. One can immediately notice that at each strain rate, if the burst displacement induced by screw dislocations is larger

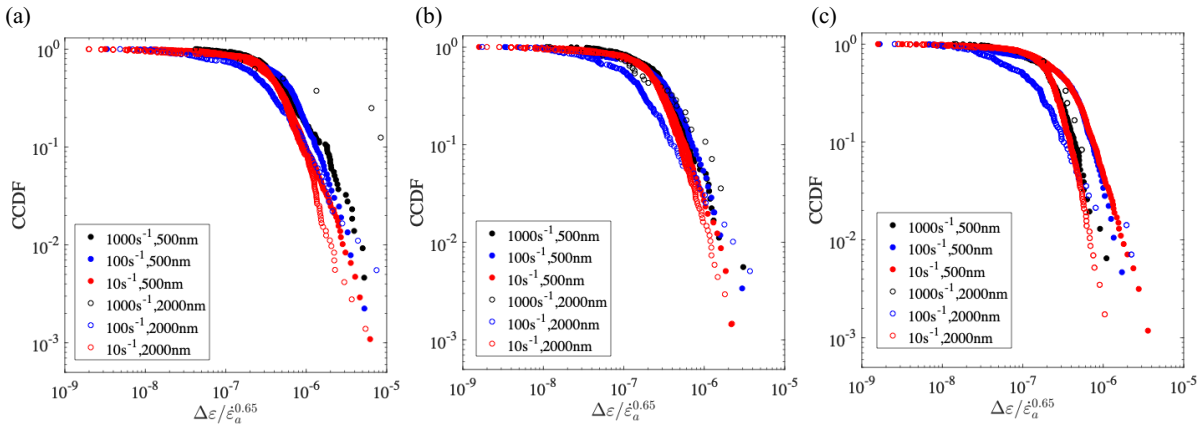

Figure 5: Statistical analysis of the burst quantity ($\Delta\varepsilon/\dot{\varepsilon}_a^{0.65}$) in compressed W pillar. $\Delta\varepsilon$ is burst strain, which is equal to $\Delta U/H$. The legend describes the pillar diameter and the applied strain rate $\dot{\varepsilon}_a$. (a) Actual strain burst distinguished by $\dot{\varepsilon}^p$, (b) virtual strain burst induced by screw dislocations, distinguished by $\dot{\varepsilon}_s^p$, (c) virtual strain burst induced by non-screw dislocations, distinguished by $\dot{\varepsilon}_{ns}^p$.

than that due to non-screw ones, their corresponding burst duration is also longer. This is easily understood, since under constant strain rate loading conditions, the burst displacement is proportional to the burst duration when the applied strain rate (displacement rate) is fixed. It can be observed from Fig. 4 that for 2 μm-diameter pillar, at fixed probability, burst events induced by screw dislocations have larger magnitude and longer duration for all applied strain rates. This is expected because the plastic deformation in bulk-like BCC crystal is believed to be dominated by the motion of screw dislocations. However, this trend is not always true when the sample size is small. Fig. 3 demonstrates that for a pillar with diameter 500 nm at higher strain rate, the burst events induced by screw dislocations have larger magnitude and longer duration, compared with the non-screw dislocations. In contrast, at lower strain rate, the burst events induced by screw dislocations have smaller magnitude and shorter duration. Namely, the non-screw dislocations contribute more to the actual burst displacement magnitude at low strain rate, as shown in Fig. 3(a).

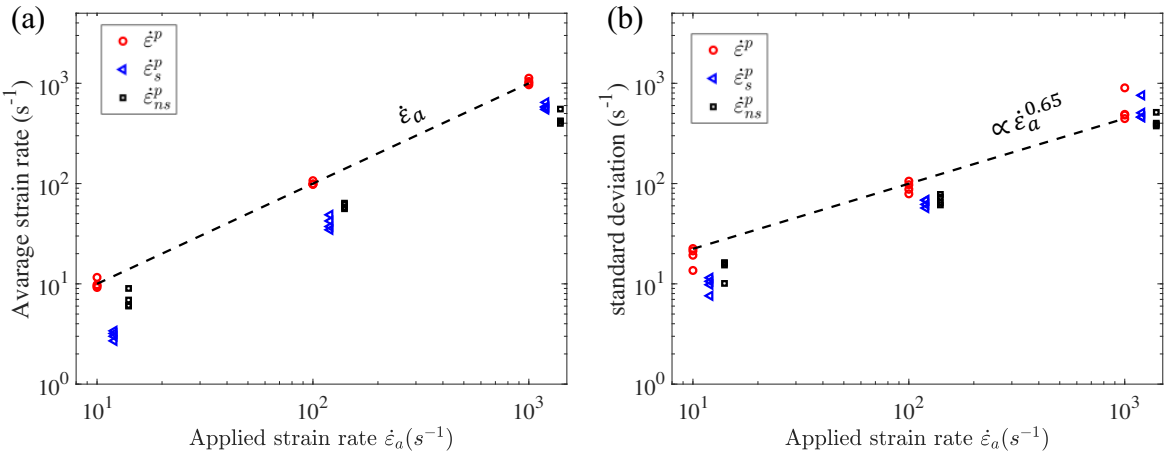

Figure 6: Average value and standard deviation of plastic strain rate $\dot{\varepsilon}^p$, $\dot{\varepsilon}_s^p$, and $\dot{\varepsilon}_{ns}^p$. The dotted line in (a) is $\dot{\varepsilon}_a$, and in (b) is proportional to $\dot{\varepsilon}_a^{0.65}$. The data corresponding to $\dot{\varepsilon}_s^p$ and $\dot{\varepsilon}_{ns}^p$ are slightly staggered horizontally in the plot for clarity of presentation.

Similar to the actual strain burst event, the burst strain data corresponding to virtual burst events induced by screw dislocations were also found to collapse to one curve. Fig. 5 (b) shows that burst strain depends on the applied strain rate, following the power law scaling $\dot{\varepsilon}_a^{0.65}$. The data for the virtual burst event induce by non-screw dislocations in Fig. 5 (c) exhibits relatively more appreciable scatter. The plastic strain rates induced by screw dislocations $\dot{\varepsilon}_s^p$, and

non-screw dislocations $\dot{\varepsilon}^p_{ns}$ are also displayed. Fig. 6 (a-b) shows that for 500 nm-diameter W pillar, the average value and standard deviation of $\dot{\varepsilon}^p_s$ are smaller than that of $\dot{\varepsilon}^p_{ns}$ at low strain rate, but are greater than that of $\dot{\varepsilon}^p_{ns}$ at high strain rate. This is also consistent with the relative contribution of screw dislocations in strain burst magnitude at different strain rates, as shown in Fig. 3. The analysis above further demonstrates the statistical connection between burst quantity and plastic strain rate.

4.2. Slow-Fast Dynamics of Strain Bursts

To understand the role of screw dislocations on strain burst statistics at different strain rates, we further analyze here the contribution of screw dislocations to burst behavior from the perspective of burst mechanism. The evolution of dislocation configurations at different strain rates is examined. Taking the case shown in Fig. 2 as an example, Fig. 7 shows the dislocation behavior during one burst event corresponding to points A and B in Fig. 2 (d) at low strain rate. Fig. 7 clearly shows that this strain burst starts mainly due to the rapid bowing out of the edge part of the dislocation source, and stops when the moving edge dislocation annihilates at the free surface. New long and free screw dislocations are generated and left behind in the crystal. Schematic plots of the dislocation mechanism and the corresponding plastic strain rate induced by non-screw and screw dislocation are shown in Fig. 8 (a). The schematic clearly describes that the gradual motion of the pinning screw dislocation elongates the length of the non-screw dislocation until it is unstable under the instantaneous stress level. The repeated breakaway of non-screw dislocations from their pinning point leads to quasi-periodic high plastic strain rate induced by non-screw dislocations, while the multiplication of screw dislocations during source operation and the annihilation of generated edge dislocations at the free surface produce plastic strain rate fluctuations. The low mobility of screw dislocations leads to lower plastic strain rate compared with that of non-screw dislocations, which is also shown in Fig. 2 (d). Such kind of source operation process in BCC crystals is consistent with experimental observations (Caillard, 2018).

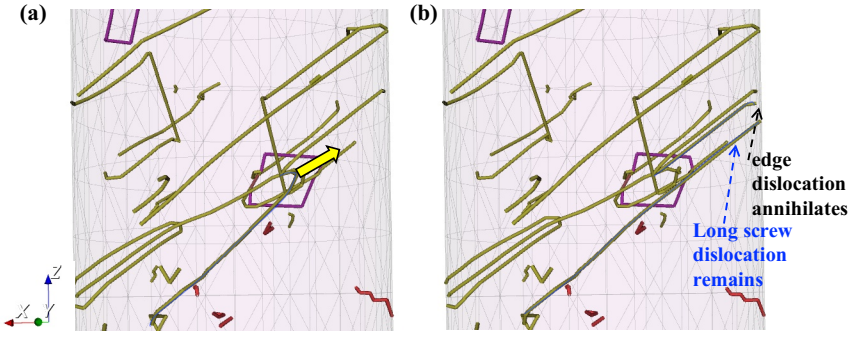

Figure 7: Strain burst mechanism at low strain rate $10s^{-1}$. Dislocation network configuration in (a) and (b) corresponds to Points A and B in Fig. 2 (d). The yellow arrows indicate the motion direction of the moving dislocations, which are highlighted using the thick transparent blue lines.

In contrast, when the applied strain rate is very high, it is very difficult or even impossible to trigger a strain burst event only through the activation of an edge dislocation. From Fig. 2 (f), many strain bursts are activated by the combined contribution of screw and non-screw dislocations. Among them, screw dislocations actually contribute more to the total plastic strain rate. The detailed evolution process of the dislocation source is schematically shown in Fig. 8 (b). One key difference from the low strain rate case is that the dislocation source is able to operate more frequently before the long free screw dislocation annihilates at the crystal surface. This condition is reached when the glide-out time for the long screw dislocation is longer than the waiting time for reactivation of the dislocation source, namely, $l/(2v_{s1}) > l_e/v_{s2}$. As shown in Fig.8 (b), l is the characteristic microstructure size (such as external size for single crystal or grain size for polycrystal), l_e is critical length of the non-screw dislocation when the dislocation source activates. v_{s1} and v_{s2} are dislocation velocities of the free long screw dislocation and the pinned screw dislocation, respectively. When the applied strain rate is high, the flow stress σ_y increases. $l_e \propto \mu b/\sigma_y$ and hence decreases. At the same time, the difference between v_{s1} and v_{s2} decreases, because the line tension force on the pinning screw dislocation plays weaker effect, when the external applied stress is higher. This means that the condition of $l/(2v_{s1}) > l_e/v_{s2}$ is easier to be met. The consequence is that more mobile screw dislocations are left in the sample, until the

multiplication process is compensated by the surface annihilation (for example, stage HI in Fig. 8 (b)). Then, the screw dislocation density stabilizes at a relatively high level, thus leading to a high plastic strain rate. One example showing a comparison of dislocation density evolution at low and high strain rates is given in Fig. 9. It can be observed that the total dislocation density is much higher at high strain rate, and that the fraction of screw dislocations is also larger at high strain rate. The equation for calculating the screw dislocation density is given in Appendix B. Fig. 10 presents the dislocation evolution process within one burst event at high strain rate, which correspond to the stage from point C to D in Fig. 2 (f). As expected, more long screw dislocations are observed. In addition, their mobility is enhanced by more frequent formation of cross-kink (see Fig. 10(b) and (c)), and the attraction and annihilation between closely-spaced screw dislocations of opposite sign (see Fig. 10 (a) and (c)). The yellow arrows in Fig. 10 indicate the motion direction of the main activated dislocation sources. One finds that that a high strain rate requires the correlated motion of multiple dislocations, instead of the discrete operation of single dislocation sources under the condition of low strain rate.

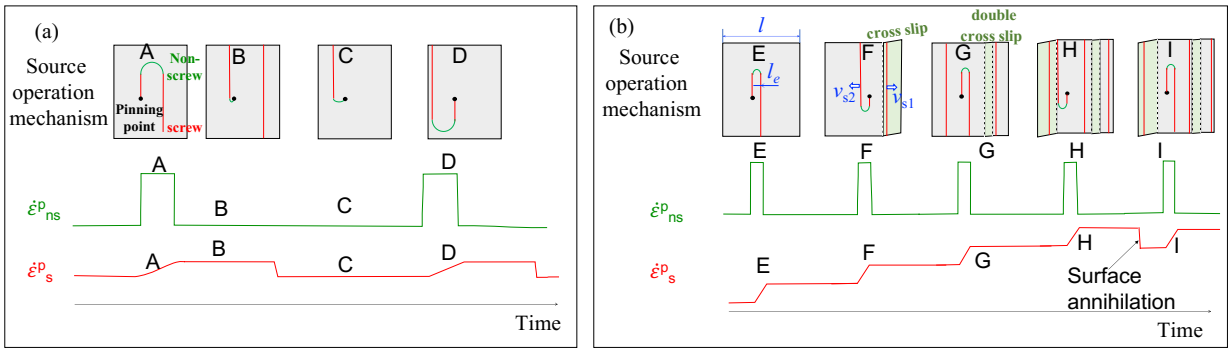

Figure 8: Schematic explaining the correspondence between source operation and plastic strain rate evolution induced by the screw dislocations and non-screw dislocations (a) at low strain rate and (b) high strain rate

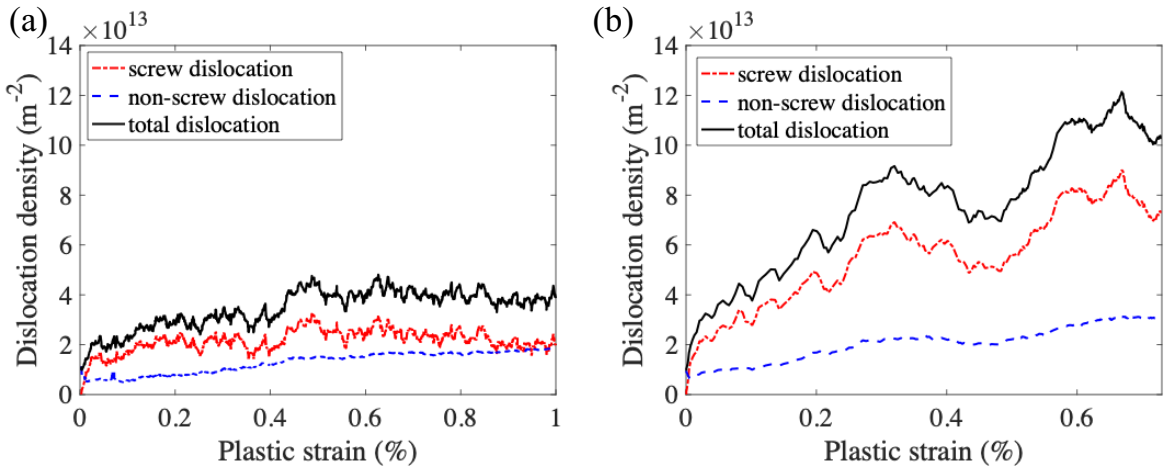

Figure 9: Evolution of dislocation density during deformation at strain rate of (a)10s^{-1} (corresponding to Fig. 2 (a)) and (b) 1000 s^{-1} (corresponding to Fig. 2(c)).

The analysis above demonstrates the role of screw dislocations in triggering strain bursts at small scales. (1) At low strain rate, the slow motion of screw dislocations first leads to the formation of unstable non-screw dislocations, while the glide of non-screw dislocations increases the mobile screw dislocation length. Such generated screw dislocations cannot be effectively stored in the sample at low strain rate, as qualitatively discussed in our previous work (Cui et al., 2016b). Therefore, the overall plastic strain rate induced by screw dislocations is smaller than that induced by non-

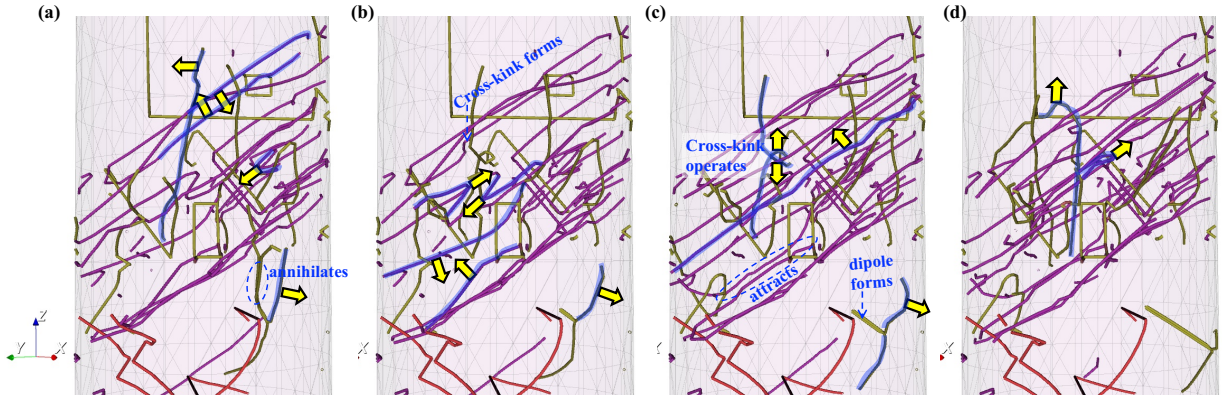

Figure 10: Strain burst mechanism at high strain rate $10^3 s^{-1}$. Dislocation configurations in (a-d) correspond to Points from C to D in Fig. 2 (f). The yellow arrows indicate the motion direction of the moving dislocations, which are highlighted using the thick transparent blue lines.

screw dislocations. The burst event is mainly controlled by the glide of non-screw dislocations. The burst duration can be approximated by the lifetime of edge dislocations t_e to bow-out of the sample, which can be estimated by l/v_e. Here, l is the characteristic length of the sample, which is set to the pillar diameter. v_e is the velocity of edge dislocation, which can be calculated according to Eq. (3). According to Fig. 1, the flow stress is about 1.5GPa for pillar with diameter 500 nm at low strain rate. The corresponding resolved shear stress for loading orientation [001] is about 0.61GPa. Thus, the corresponding lifetime is about 2ns, which can be considered as the lower bound of the lifetime. According to Fig.7, the edge dislocation is confined by the two neighboring long straight screw dislocations. If the length of the edge dislocation is expressed as l_e (as schematically shown in Fig. 8(b)), the line tension stress can be estimated as $\mu b/l_d$. Here, μ is the shear modulus, and b is the burgers vector magnitude. The corresponding estimated lifetime of edge dislocation is shown in Fig. 11. If the lattice resistance stress for edge dislocation is further considered, the effective resolved shear stress further reduces, and longer lifetime is expected. This rough estimation of the lifetime of an edge dislocation is close to the burst duration shown in Fig. 3(b). (2) For the high strain rate case, both the density and the mobility of screw dislocations are higher. Their corresponding plastic strain rate contributes more than that of non-screw dislocations. Some strain bursts are mainly induced by screw dislocations, but most of the strain burst needs to be triggered by the collective effect of both the screw and non-screw parts of dislocations. A higher flow stress leads to shorter lifetime for edge dislocations to glide-out of the free surface. At the same time, the surface annihilation of either screw or edge dislocations may lead to the shutdown of one burst event, leading to a shorter burst duration at higher strain rate, as shown in Fig. 3 (b).

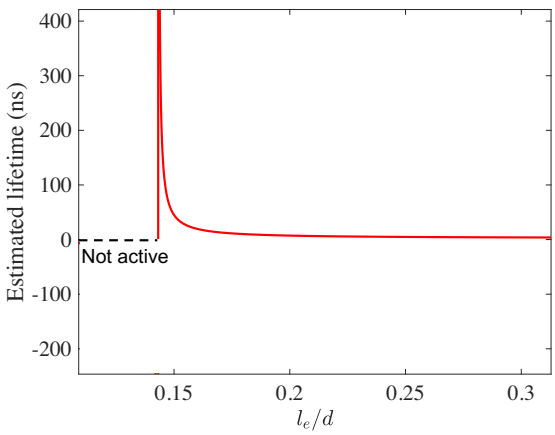

Figure 11: Estimated lifetime of an edge dislocation as a function of edge dislocation length l_e normalized by pillar diameter d

4.3. *Effects of Screw Dislocations on Spatial Distributions*

In the spatial domain, the existence of numerous long screw dislocations provides the necessary condition of the occurrence of cross slip. This is expected to contribute to a more homogeneous distribution of plastic deformation (Cui et al., 2018a). Taking the case of one single dislocation source, schematically shown in Fig. 8 (b) as an example, many long screw dislocations are produced due to continuous source operation before they annihilate at the surface. Frequent cross-slip events of long screw dislocations can avoid the strong dislocation pile-up effect, as schematically shown in Fig. 8 (b). Therefore, the source strength does not significantly increase, even with many long screw dislocations left. One example of the actual dislocation source operation process at strain rate $10^3 s^{-1}$ is given in Fig. 12. In a W-cube with side length 500 nm, there is initially only one dislocation loop, with two sessile segments AB and CD and two mobile segments AC and BD, as shown in Fig. 12(a). With an increase of the applied stress, Frank-Read sources AC and BD bow out around the pinning points A, B, C, and D. Then, four single arm sources are generated due to surface truncation effects, as indicated by the transparent thick lines in Fig. 12(b). In simulations using complicated dislocation structures, sessile dislocation junctions, or strong dislocation entanglement can also provide pinning points. Single-arm source mechanisms are widely observed in the simulations.

After multiple times of single-arm dislocation source operation as schematically shown in Fig. 8, numerous long screw dislocations are generated, as shown in Fig. 12(b). The slipped area information of the dislocation source corresponding to the state shown in Fig. 12(b) is given in Fig. 12(c). A clear wavy slip feature is observed due to the frequent occurrence of cross slip of screw dislocations, as explained in Fig. 8 (b). The plastic deformation regime significantly widens due to cross-slip events.

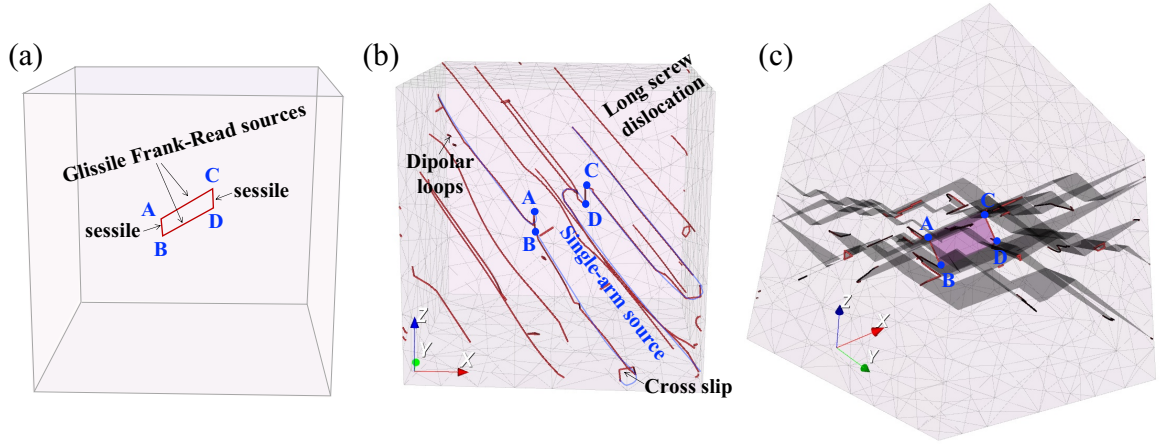

Figure 12: Single-arm source operation in a W-cube with side length 500 nm at strain rate $10^3 s^{-1}$. (a) initial dislocation configuration containing two Frank-Read sources AC and BD. Dislocation segments AB and CD are sessile dislocations, so points A, B, C and D are pinning points. (b) One snapshot of dislocation configuration during source operation, four thick transparent blue lines indicate four single-arm sources, (c) the corresponding slipped area is shaded from another viewpoint.

The frequent cross-slip and the formation of multiple dislocation jogs leads to the formation of small dipolar loops, such as indicated in Fig. 12(b). This is one typical feature of dislocation configurations in BCC crystals. The detailed formation mechanism of dipolar loops is given in Fig.11 in (Cui et al., 2016b) and Fig. 3 in (Hsiung, 2010). We take one set of simulations as an example, which contains the same initial dislocation configuration. The number of dipolar loops during the deformation stage at different strain rates are qualitatively evaluated, as shown in Fig. 13. The annihilation of some dipolar loops during the deformation process is due to their interaction with glide dislocations. It is found that the number of small dipolar loop is much higher at higher strain rate. This is the consequence of higher screw dislocation density, the more frequent cross-slip and jog formation. Such higher number of dipolar loops at higher strain rate is also observed experimentally in BCC Mo and Ta (Hsiung and Lassila, 2000; Hsiung, 2010). Note that the burst statistics is also influenced by the occurrence of cross-slip. For example, compared with the case without cross-slip, burst size is expected to be larger with cross slip because cross-slip increases the mean free path of the dislocation before it annihilates from free surface or being trapped by the slow screw dislocations. In addition,

cross-kink formation also contributes to more significant dislocation multiplication. Therefore, it is easier to trigger more correlated dislocation motion with the help of cross-slip, as discussed in (Crosby et al., 2015).

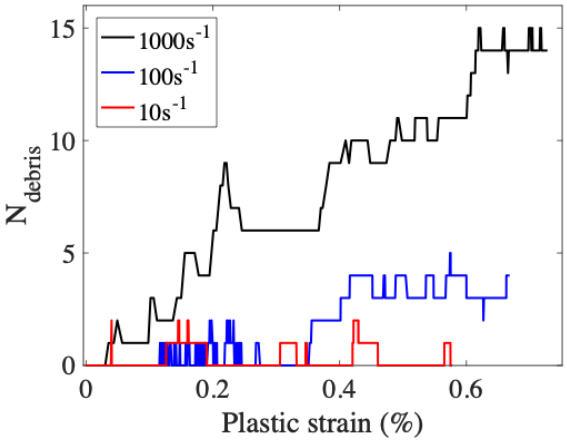

Figure 13: Evolution of dislocation debris number N_{debris} at different strain rates

To further evaluate the spatial distribution of plastic deformation, the slipped area of dislocations that have moved, and the plastic strain distribution are analyzed. As an example, Fig. 14 gives the slipped area corresponding to a given plastic strain amount 0.5%. Fig. 14 (a-b) and (e-f) correspond to the slipped area from two viewpoints at lower strain rate and higher strain rate, respectively. The extent of the shaded color is proportional to the number of times the slipped area was swept by moving dislocations. It can be observed that the distribution of the slipped area is comparatively more expanded at higher strain rate. This implies that more slip systems are activated at higher strain rate.

The improved simulation method allows us to further calculate the local plastic strain distribution, according to the local slipped area information. The uniqueness of this calculation is that the spatial resolution of the local plastic strain calculation can be as high as desired. Because the calculation is reproduced based on the slipped area information as described in section 2, the spatial resolution of the calculation is independent of the mesh size of the finite element method, which is not the case in previous eigen-strain formulations. In Fig. 14 (c) and (g), the local plastic strain distribution on an xz-cutting plane with y=0 is presented. The spatial resolution of 20 b is used. Here, b is the magnitude of Burgers vector. If one considers the process that dislocation swept the slip area for one time, the difference between averaged plastic strain increment (using the whole volume of the sample) and the local plastic strain increment (using the local layer around the slipped area) is approximately equal to the sample height divided by the spatial resolution. Fig. 14 (c) and (g) clearly shows the intersection lines of the slip area with the cutting plane. Frequent cross-slip is also observed. At low strain rate, a clearer shear band is observed, implying higher extent of deformation localization. Furthermore, Fig. 14 (d) and (h) show the deformed configuration corresponding to Fig. 14 (c) and (g) with displacement magnified by a factor of 40. The surface steps are clearly observed, with a high resolution. Fig. 14 (d) exhibits more localized deformation feature near the center region of the sample, compared to Fig. 14 (h). This is consistent with our experimental observation shown in Fig. 1 (b) for pillar with diameter 500nm. The deformation is comparably more localized at low strain rate compared with that at high strain rate. With respect to W pillar with diameter 2000nm in Fig. 1 (b), more smooth deformed morphology is observed and no clear difference is observed for the considered cases of low strain rate and high strain rate.

5. Summary & Conclusions

In summary, systematic 3D-DDD simulations were carried out to understand the role of slow screw dislocations on rapid strain burst events in submicron BCC W, in particular on the temporal and spatial distributions of plastic strain. The current improved 3D-DDD simulation method leads to accurate calculations of the slipped area of moving

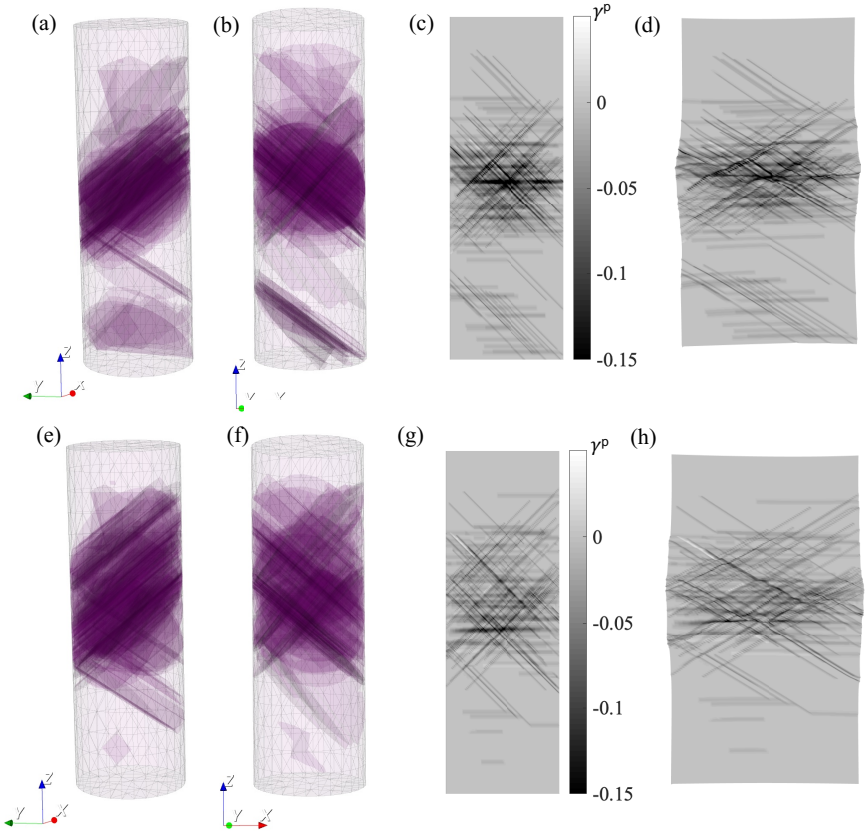

Figure 14: Slipped area in compressed W pillars, (a-b) at strain rate $10s^{-1}$ and (e-f) at strain rate $10^3 s^{-1}$. Distribution of plastic strain ε^p on xz plane (y=0), (c-d) at strain rate $10s^{-1}$ and (g-h) at strain rate $10^3 s^{-1}$. In (c) and (g) the deformation shape is not shown, in (d) and (h) the displacement is magnified by a factor of 40.

dislocations, the plastic strain rate, and the displacement field. These are all important features required to accurately distinguish the strain burst event, and to understand the spatial distribution of the plastic strain and displacement with high spatial resolution. Comparison of the 3D-DDD simulation results with experimental data validated the effectiveness of the simulation methodology.

The following conclusions are drawn from the present investigation.

1. Strain burst magnitude exhibits strain rate dependence, and scales as $\dot{\varepsilon}_a^{0.65}$. Interestingly, the standard deviation of the plastic strain rate is also found to exhibit a similar power law scaling with $\dot{\varepsilon}_a^{0.65}$. The mean value of plastic strain rate is almost equal to $\dot{\varepsilon}_a$, implying that there is no overall hardening and softening for the considered strain range.
2. For 2 μm-diameter W-pillar, the strain burst event is dominated by slow screw dislocation behavior. The virtual strain burst magnitude induced by screw dislocations is larger than that induced by non-screw components. In contrast, for 500 nm-diameter W pillar, the rapid glide of non-screw dislocations is the main reason for triggering strain bursts at low strain rates, while screw dislocations play a more important role in influencing the strain burst at high strain rate. This is explained through different features of dislocation source operation, depending on the strain rate. At high strain rate and flow stress, frequent cross-slip and jog multiplication lead to rapid and frequent dislocation multiplication. This further contributes to the effective storage of screw dislocations before surface annihilation, increasing the overall plastic strain rate induced by screw dislocations.
3. Screw dislocations are found to contribute to frequent cross-slip and jog multiplication, inducing spatially homogeneous plastic deformation and wider slip bands at high strain rate. The 3D slip area distribution and the

plastic strain distribution on a cutting-plane clearly demonstrate this trend. In addition, the number of small dislocation debris, as a result of cross-slip and jog multiplication, also increases with the strain rate, which is consistent with experimental observations.

In the present work, our focus is on the role of screw dislocation on strain burst under different strain rates. The temperature effects are also expected to have a strong effect as discussed in the introduction part (Cui et al., 2016b; Le et al., 2017). Taking the extreme case as an example, when the temperature is very high, the mobility of screw dislocations becomes similar to that of edge dislocations. In this case, the plastic behavior of BCC crystals becomes similar to that of face centered cubic (FCC) crystals. Recent experimental work compares the strain burst behavior of BCC Nb and FCC Au (Sparks and Maaß, 2018b). The avalanche velocity relaxation is found to be significantly different, because the screw-limited avalanche dynamics leads to a slower velocity decay in Nb. Therefore, temperature is expected to control the role of screw dislocation on strain burst behavior, which is reserved for future dedicated studies. Furthermore, in an age of data-based science, further dedicated efforts are required to connect the modern machine learning technique and 3D microstructure evolution information, which may contribute to new insights in understanding the deformation mechanisms and developing underpinning theoretical models.

Acknowledgments

This material is based upon work supported by the National Science Foundation, Grant Numbers CMMI-1024353 and CMMI-1727740 at UCLA.

Appendix A Basic idea of calculating local plastic strain in 3D DDD

According to the Orowan's relation, the plastic strain is proportional to the slipped area of the moved dislocation. Therefore, accurately calculating the slipped area is an essential step in determining the plastic strain distribution. Generally, in DDD, only the dislocation segment information is stored, as shown in Fig. A1(a). This cannot give deterministic slipped area information. For example, the dislocation loop ADBC in Fig. A1(a) may be formed due to the expansion of a tiny dislocation loop nucleated inside the crystal. The corresponding slipped area is shaded in Fig. A1(b). Alternatively, the dislocation loop ADBC may be formed due to surface nucleation and the subsequent glide. The corresponding slipped area is the shaded area in Fig. A1(c). Segments EFGHIJE in Fig. A1(c) represents the annihilated dislocation segment at the free surfaces.

To solve this problem, we retain the dislocation loop as well as the segment/node features (i.e. duality of representation) in our new version of the simulation method. The areas inside the dislocation loops can directly determine their slipped areas, if the condition that each loop only belongs to one slip plane is met. The generality of this method is illustrated through one example of a cross-slipped dislocation loop. Imagine that one dislocation segment AB in loop ABCA cross slip to another slip plane, as shown in Fig. A1(b). Then a new dislocation loop ADBA is generated, which belongs to a new slip plane. Because the segment AB in loop ABCA and the segment BA in loop ADBA have the same Burgers vector and opposite line directions, their sum represents a zero Burgers vector segment, which neither contributes to the stress field nor participates in dislocation interactions. Therefore, the physical dislocation segment information shown in Fig. A1(b) is the same as that shown in Fig. A1(a). A similar treatment can also be used to represent the dislocation junction segment. The only difference is that the sum of the shared segment of two neighboring dislocation loops has non-zero Burgers vector. With respect to the other case shown in Fig. A1(c), two dislocation loops AEFGHBCA and EADBHIJE are stored. It is very straightforward to determine the corresponding enclosed slipped area (shaded in the figure). The sum of the segment AE in loop AEFGHBCA and the segment EA in loop EADBHIJE, as well as the sum of the segment HB in loop AEFGHBCA and the segment BH in loop EADBHIJE, have the zero Burgers vector. The surface segments EFGHIJE does not contribute to the stress field and dislocation interaction. Therefore, the physical dislocation segment information shown in Fig. A1(c) is also the same as that shown in Fig. A1(a). This example illustrates that the dislocation loop information can help to get the deterministic slipped area information. This is important not only for calculating plastic strain distributions, but also for calculating the displacement field induced by dislocation motion. More details of these new features of the simulation method and its advantages will be presented in a subsequent dedicated paper.

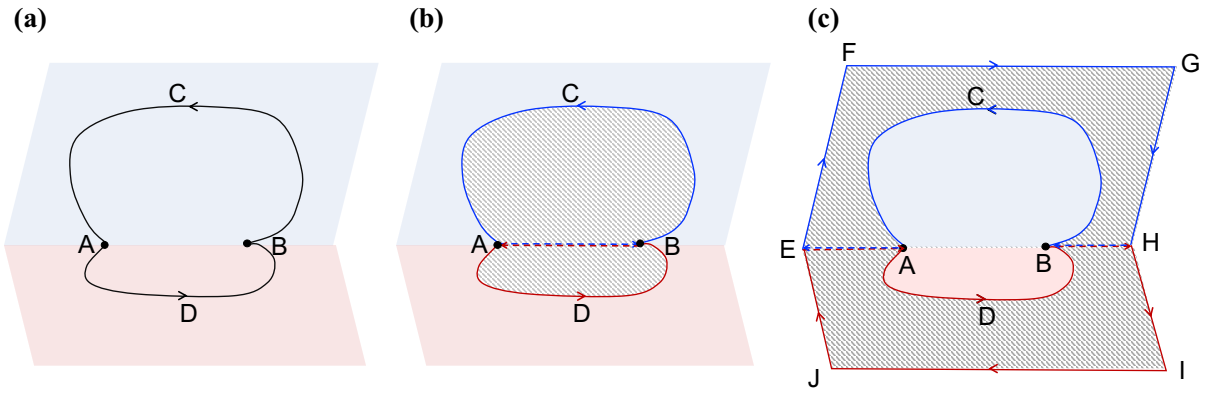

Figure A1: (a) If only the dislocation segment features are retained, the corresponding slipped area is not determined; (b-c) If both the dislocation loop and the segment features are retained, the enclosed areas by the loops determine the slipped areas, which correspond to the shaded region. The arrows describe the line direction of the dislocation segment.

Appendix B Weight function of screw dislocation

In order to separate out the contribution of screw dislocation in plastic strain rate, the virtual strain rate due to the motion of non-screw dislocations $\dot{\varepsilon}^p_{ns}$ and the virtual strain rate due to the motion of screw dislocations $\dot{\varepsilon}^p_s$ are calculated as,

$$\begin{aligned} \dot{\varepsilon}^p_{ns} &= \sum_{i=1}^{N_{dis}} \dot{\varepsilon}^p_{(i)} \cdot k(\theta_{(i)}) \\ \dot{\varepsilon}^p_s &= \sum_{i=1}^{N_{dis}} \dot{\varepsilon}^p_{(i)} \cdot (1 - k(\theta_{(i)})) \end{aligned} \tag{B.1}$$

where $\dot{\varepsilon}^p_{(i)}$ is the plastic strain rate induced by the ith dislocation segment, and $\theta_{(i)}$ is the angle between the tangent direction and the Burgers vector direction of the ith dislocation segment. $k(\theta_{(i)})$ is a dimensionless weight function with properties $\lim_{\theta\to 0} k(\theta) = 0$, and $\lim_{\theta\to\pi/2} k(\theta) = 1$. In 3D DDD, a dislocation segment is generally recognized as screw dislocation, when $\theta_{(i)}$ is smaller than a critical angle θ_c due to the existence of numerical roundoff errors. In this case, $k(\theta_{(i)})$ is taken as a Heaviside function. Namely, if $\theta_{(i)} < \theta_c$, $k(\theta_{(i)}) = 0$, otherwise, $k(\theta_{(i)}) = 1$. However, till now, there is no well-accepted strict way to determine the critical angle θ_c. To avoid the artificiality of introducing a critical angle θ_c, $k(\theta_{(i)})$ is taken as $sin^2\theta_{(i)}$ in the current work.

The relation $k(\theta_{(i)}) = sin^2\theta_{(i)}$ can be rationalized based on simple geometric relations as shown in Fig. B1. Imagine that there is an infinitely short curved dislocation line, it can be decomposed into a non-screw part and a screw part. We would like to conserve the swept area rate of a curved segment with the approximate non-screw and screw components. According to Fig. B1, the swept area of the mixed dislocation line is approximately equal to the sum of the swept areas of the non-screw part and the swept area of the screw part, expressed as follows,

$$\vec{v}\,\mathrm{d}t \times \vec{L}_m = \vec{v}\,\mathrm{d}t \times \vec{L}_{ns} + \vec{v}\,\mathrm{d}t \times \vec{L}_s \tag{B.2}$$

where the variables with superposed arrow represent vectors, whose corresponding magnitudes are expressed by the same symbol without a superposed arrow. $\times$ represents cross product of a vector. dt is time increment. $\vec{v}$ represents the velocity vector of dislocation. $\vec{L}_{ns}$, $\vec{L}_s$, and $\vec{L}_m$ represent the tangent direction vector of non-screw part, screw part and mixed dislocation, respectively. According to Fig. B1, the non-screw part means the edge part for the considered case.

Since the plastic distortion rate is proportional to the swept area rate, the plastic strain rate induced by a non-screw dislocation $\dot{\varepsilon}^p_{ns}$ and the plastic strain rate induced by a screw dislocation $\dot{\varepsilon}^p_{s}$ for the ith dislocation segment can be calculated as follows,

$$\begin{aligned}
\frac{\dot{\varepsilon}^p_{ns(i)}}{\dot{\varepsilon}^p_{(i)}} &= \frac{\overrightarrow{v}\,\mathrm{d}t \times \overrightarrow{L}_{ns}}{\overrightarrow{v}\,\mathrm{d}t \times \overrightarrow{L}_{m}} = \frac{vdtsin(\pi - \theta_{(i)})L_{ns}}{vdtL_m} = \frac{sin\theta_{(i)}L_{ns}}{L_m} = sin^2\theta_{(i)} \\
\frac{\dot{\varepsilon}^p_{s(i)}}{\dot{\varepsilon}^p_{(i)}} &= \frac{\overrightarrow{v}\,\mathrm{d}t \times \overrightarrow{L}_{s}}{\overrightarrow{v}\,\mathrm{d}t \times \overrightarrow{L}_{m}} = \frac{vdtsin(\pi/2 - \theta_{(i)})L_{s}}{vdtL_m} = \frac{cos\theta_{(i)}L_{s}}{L_m} = cos^2\theta_{(i)}
\end{aligned} \tag{B.3}$$

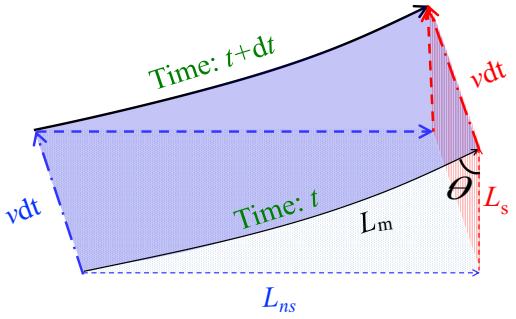

Figure B1: Schematic showing the slip of a mixed dislocation. Here, L_m, L_s and L_{ns} indicate the dislocation line, the screw part and the non-screw part, respectively. The thin lines correspond to time step t, and the thick lines correspond to time step $t + dt$.

According to Eq. (B.1) and Eq. (B.3), $k(\theta_{(i)})$ is taken as $sin^2\theta_{(i)}$. This weight function of screw dislocation is consistent with the weight function used in the dislocation mobility law given in Eq. (1).

For consistency, the screw-part dislocation density ρ_s and the non-screw-part dislocation density ρ_{ns} in Fig. 9 are also calculated using,

$$\begin{aligned}
\rho_s &= \sum_{i=1}^{N_{dis}} \frac{L_{m(i)} sin^2\theta_{(i)}}{V} \\
\rho_{ns} &= \sum_{i=1}^{N_{dis}} \frac{L_{m(i)} cos^2\theta_{(i)}}{V}
\end{aligned} \tag{B.4}$$

where V is the volume. Eq. (B.4) meets the condition that $\rho = \rho_{ns} + \rho_s$. When the curved dislocation line is short enough, $L_m = \sqrt{L_{ns}^2 + L_s^2} \neq L_{ns} + L_s$. Therefore, it is not reasonable to use $\rho_s = \sum_{i=1}^{N_{dis}} \frac{L_{s(i)}}{V}$. The definition of Eq. (B.4) reflects the effect of dislocation density in virtual plastic strain rate when the effect of velocity difference between screw dislocation and non-screw dislocation is ignored.

References

Brechtl, J., S. Chen, X. Xie, Y. Ren, J. Qiao, P. Liaw, and S. Zinkle (2019). Towards a greater understanding of serrated flows in an al-containing high-entropy-based alloy. *International Journal of Plasticity 115*, 71–92.

Brinckmann, S., J.-Y. Kim, and J. R. Greer (2008). Fundamental differences in mechanical behavior between two types of crystals at the nanoscale. *Phys. Rev. Lett. 100*(15), 155502.

Caillard, D. (2018). Geometry and kinetics of glide of screw dislocations in tungsten between 95k and 573k. *Acta Materialia 161*, 21–34.

Cao, L. and M. Koslowski (2015, JUN 28). Rate-limited plastic deformation in nanocrystalline Ni. *JOURNAL OF APPLIED PHYSICS 117*(24).

Cereceda, D., M. Diehl, F. Roters, D. Raabe, J. M. Perlado, and J. Marian (2016). Unraveling the temperature dependence of the yield strength in single-crystal tungsten using atomistically-informed crystal plasticity calculations. *International Journal of Plasticity 78*, 242–265.

Chen, S. R. and G. T. Gray III (1995). Constitutive behavior of tungsten and tantalum: experiments and modeling. In *Proceedings of the 2nd international conference on tungsten and refractory metals, metal powders industries federation, Princeton, New Jersey*, pp. 489–498.

Crosby, T., G. Po, C. Erel, and N. Ghoniem (2015). The origin of strain avalanches in sub-micron plasticity of fcc metals. *ACTA MATERIALIA 89*, 123–132.

Csikor, F. F., C. Motz, D. Weygand, M. Zaiser, and S. Zapperi (2007). Dislocation avalanches, strain bursts, and the problem of plastic forming at the micrometer scale. *Science 318*(5848), 251–254.

Cui, Y., P. Lin, Z. Liu, and Z. Zhuang (2014). Theoretical and numerical investigations of single arm dislocation source controlled plastic flow in fcc micropillars. *International Journal of Plasticity 55*, 279–292.

Cui, Y., Z. Liu, and Z. Zhuang (2015). Quantitative investigations on dislocation based discrete-continuous model of crystal plasticity at submicron scale. *International Journal of Plasticity 69*, 54–72.

Cui, Y., G. Po, and N. Ghoniem (2016a). Controlling strain bursts and avalanches at the nano-to micrometer scale. *Physical Review Letters 117*(15), 155502.

Cui, Y., G. Po, and N. Ghoniem (2016b). Temperature insensitivity of the flow stress in body-centered cubic micropillar crystals. *Acta Materialia 108*, 128–137.

Cui, Y., G. Po, and N. Ghoniem (2017). Influence of loading control on strain bursts and dislocation avalanches at the nanometer and micrometer scale. *Physical Review B 95*(6), 064103.

Cui, Y., G. Po, and N. Ghoniem (2018a). Size-Tuned Plastic Flow Localization in Irradiated Materials at the Submicron Scale. *PHYSICAL REVIEW LETTERS 120*(21).

Cui, Y., G. Po, and N. M. Ghoniem (2018b). A coupled dislocation dynamics-continuum barrier field model with application to irradiated materials. *International Journal of Plasticity 104*, 54–67.

Dümmer, T., J. Lasalvia, G. Ravichandran, and M. Meyers (1998). Effect of strain rate on plastic flow and failure in polycrystalline tungsten. *Acta Materialia 46*(17), 6267–6290.

Fressengeas, C., A. Beaudoin, D. Entemeyer, T. Lebedkina, M. Lebyodkin, and V. Taupin (2009). Dislocation transport and intermittency in the plasticity of crystalline solids. *Phys. Rev. B 79*(1), 014108.

Ghoniem, N., M, S.-H. Tong, and L. Sun (2000). Parametric dislocation dynamics: a thermodynamics-based approach to investigations of mesoscopic plastic deformation. *Physical Review B 61*(2), 913.

Ghoniem, N. M. and L. Sun (1999). Fast-sum method for the elastic field of three-dimensional dislocation ensembles. *Physical Review B 60*(1), 128.

Hsiung, L. and D. Lassila (2000). Initial dislocation structure and dynamic dislocation multiplication in mo single crystals. Technical report, Lawrence Livermore National Lab., CA (US).

Hsiung, L. L. (2010). On the mechanism of anomalous slip in bcc metals. *Materials Science and Engineering: A 528*(1), 329–337.

Huang, M., J. Tong, and Z. Li (2014). A study of fatigue crack tip characteristics using discrete dislocation dynamics. *International Journal of Plasticity 54*, 229–246.

Jamond, O., R. Gatti, A. Roos, and B. Devincre (2016). Consistent formulation for the discrete-continuous model: Improving complex dislocation dynamics simulations. *International Journal of Plasticity 80*, 19–37.

Kaufmann, D., A. Schneider, R. Mönig, C. Volkert, and O. Kraft (2013). Effect of surface orientation on the plasticity of small bcc metals. *International Journal of Plasticity 49*, 145–151.

Kiener, D. and A. Minor (2011). Source-controlled yield and hardening of cu (100) studied by in situ transmission electron microscopy. *Acta Mater. 59*(4), 1328–1337.

Kositski, R. and D. Mordehai (2015). Depinning-controlled plastic deformation during nanoindentation of bcc iron thin films and nanoparticles. *Acta Materialia 90*, 370–379.

Krebs, J., S. Rao, S. Verheyden, C. Miko, R. Goodall, W. Curtin, and A. Mortensen (2017). Cast aluminium single crystals cross the threshold from bulk to size-dependent stochastic plasticity. *Nature materials 16*(7).

Langer, J. (2006). Shear-transformation-zone theory of deformation in metallic glasses. *Scripta Materialia 54*(3), 375 – 379. Viewpoint set no: 37. On mechanical behavior of metallic glasses.

Langer, J. and L. Pechenik (2003, DEC). Dynamics of shear-transformation zones in amorphous plasticity: Energetic constraints in a minimal theory. *PHYSICAL REVIEW E 68*(6, 1).

Langer, J. S., E. Bouchbinder, and T. Lookman (2010, JUN). Thermodynamic theory of dislocation-mediated plasticity. *ACTA MATERIALIA 58*(10), 3718–3732.

Le, K. C., T. M. Tran, and J. S. Langer (2017, JUL 12). Thermodynamic dislocation theory of high-temperature deformation in aluminum and steel. *PHYSICAL REVIEW E 96*(1).

Lehtinen, A., G. Costantini, M. J. Alava, S. Zapperi, and L. Laurson (2016). Glassy features of crystal plasticity. *Physical Review B 94*(6), 064101.

Lemarchand, C., B. Devincre, and L. Kubin (2001). Homogenization method for a discrete-continuum simulation of dislocation dynamics. *Journal of the Mechanics and Physics of Solids 49*(9), 1969–1982.

Lim, H., L. Hale, J. Zimmerman, C. Battaile, and C. Weinberger (2015). A multi-scale model of dislocation plasticity in α-fe: Incorporating temperature, strain rate and non-schmid effects. *International Journal of Plasticity 73*, 100–118.

Liu, F., Z.-l. Liu, P. Lin, and Z. Zhuang (2017). Numerical investigations of helical dislocations based on coupled glide-climb model. *International Journal of Plasticity 92*, 2–18.

Maaß, R. and P. Derlet (2018). Micro-plasticity and recent insights from intermittent and small-scale plasticity. *Acta Materialia 143*, 338–363.

Maaß, R., M. Wraith, J. Uhl, J. Greer, and K. Dahmen (2015). Slip statistics of dislocation avalanches under different loading modes. *Phys. Rev. E 91*(4), 042403.

Ni, X., S. Papanikolaou, G. Vajente, R. X. Adhikari, and J. R. Greer (2017). Probing microplasticity in small-scale fcc crystals via dynamic mechanical analysis. *Physical review letters 118*(15), 155501.

Papanikolaou, S., Y. Cui, and N. Ghoniem (2017). Avalanches and plastic flow in crystal plasticity: an overview. *Modelling and Simulation in Materials Science and Engineering 26*(1), 013001.

Po, G., Y. Cui, D. Rivera, D. Cereceda, T. D. Swinburne, J. Marian, and N. Ghoniem (2016). A phenomenological dislocation mobility law for bcc metals. *Acta Materialia 119*, 123–135.

Po, G. and N. Ghoniem (2015). Mechanics of defect evolution library, model. ⟨*https://bitbucket.org/model/model/wiki/home*⟩.

Po, G., M. S. Mohamed, T. Crosby, C. Erel, A. El-Azab, and N. Ghoniem (2014). Recent progress in discrete dislocation dynamics and its applications to micro plasticity. *JOM 66*(10), 2108–2120.

Rao, S. I., D. Dimiduk, T. A. Parthasarathy, M. Uchic, M. Tang, and C. Woodward (2008). Athermal mechanisms of size-dependent crystal flow gleaned from three-dimensional discrete dislocation simulations. *Acta Mater. 56*(13), 3245–3259.

Salmenjoki, H., M. J. Alava, and L. Laurson (2018). Machine learning plastic deformation of crystals. *Nature communications 9*(1), 5307.

Sills, R. B., N. Bertin, A. Aghaei, and W. Cai (2018). Dislocation networks and the microstructural origin of strain hardening. *Physical review letters 121*(8), 085501.

Song, H., H. Yavas, E. Van der Giessen, and S. Papanikolaou (2019a). Discrete dislocation dynamics simulations of nanoindentation with pre-stress: Hardness and statistics of abrupt plastic events. *JOURNAL OF THE MECHANICS AND PHYSICS OF SOLIDS 123*(SI), 332–347.

Song, H., D. Dimiduk, and S. Papanikolaou (2019b). Universality Class of Nanocrystal Plasticity: Localization and Self-Organization in Discrete Dislocation Dynamics. *PHYSICAL REVIEW LETTERS 122*(17).

Sparks, G., Y. Cui, G. Po, R. Rizzardi, J. Marian, and R. Maaß (2019). Intermittent-to-smooth-transition in microplasticity. *Submitted*.

Sparks, G. and R. Maaß (2018a). Nontrivial scaling exponents of dislocation avalanches in microplasticity. *Physical Review Materials 2*(12), 120601.

Sparks, G. and R. Maaß (2018b). Shapes and velocity relaxation of dislocation avalanches in au and nb single crystals. *Acta Materialia*.

Srivastava, K., R. Groeger, D. Weygand, and P. Gumbsch (2013, AUG). Dislocation motion in tungsten: Atomistic input to discrete dislocation simulations. *INTERNATIONAL JOURNAL OF PLASTICITY 47*, 126–142.

Srivastava, P., Y. Cui, K. Jiang, V. Gupta, and N. Ghoniem (2019). Strain rate dependent flow stress, strain hardening rate, and dislocation avalanches in nano-scaled and micron-scaled tungsten. In preparation.

Uhl, J. T., S. Pathak, D. Schorlemmer, X. Liu, R. Swindeman, B. A. Brinkman, M. LeBlanc, G. Tsekenis, N. Friedman, R. Behringer, et al. (2015). Universal quake statistics: From compressed nanocrystals to earthquakes. *Sci. Rep. 5*, 16493.

Vadalakonda, S., R. Banerjee, A. Puthcode, and R. Mirshams (2006). Comparison of incipient plasticity in bcc and fcc metals studied using nanoindentation. *Materials Science and Engineering: A 426*(1-2), 208–213.

Vattré, A., B. Devincre, F. Feyel, R. Gatti, S. Groh, O. Jamond, and A. Roos (2014). Modelling crystal plasticity by 3d dislocation dynamics and the finite element method: the discrete-continuous model revisited. *Journal of the Mechanics and Physics of Solids 63*, 491–505.

Wang, M. and A. Ngan (2004). Indentation strain burst phenomenon induced by grain boundaries in niobium. *Journal of materials research 19*(8), 2478–2486.

Wang, P., F. Liu, Y. Cui, Z. Liu, S. Qu, and Z. Zhuang (2018). Interpreting strain burst in micropillar compression through instability of loading system. *International Journal of Plasticity 107*, 150–163.

Weiss, J., T. Richeton, F. Louchet, F. Chmelik, P. Dobron, D. Entemeyer, M. Lebyodkin, T. Lebedkina, C. Fressengeas, and R. J. McDonald (2007). Evidence for universal intermittent crystal plasticity from acoustic emission and high-resolution extensometry experiments. *Physical review B 76*(22), 224110.

Yu, H., A. Cocks, and E. Tarleton (2019). Discrete dislocation plasticity helps understand hydrogen effects in bcc materials. *Journal of the Mechanics and Physics of Solids 123*, 41–60.

Zaiser, M. (2006). Scale invariance in plastic flow of crystalline solids. *Adv. Phys. 55*(1-2), 185–245.

Zaiser, M., J. Schwerdtfeger, A. Schneider, C. Frick, B. G. Clark, P. Gruber, and E. Arzt (2008). Strain bursts in plastically deforming molybdenum micro-and nanopillars. *Philos. Mag. 88*(30-32), 3861–3874.

Zhang, J., K. Kishida, and H. Inui (2017). Specimen size and shape dependent yield strength in micropillar compression deformation of mo single crystals. *International Journal of Plasticity 92*, 45–56.

Zhang, X., X. Zhang, F. Shang, and Q. Li (2016). Second-order work and strain burst in single-crystalline micropillar plasticity. *International Journal of Plasticity 77*, 192–213.

Zhao, L., Q. Guo, Z. Li, Z. Li, G. Fan, D.-B. Xiong, Y. Su, J. Zhang, Z. Tan, and D. Zhang (2018). Strain-rate dependent deformation mechanism of graphene-al nanolaminated composites studied using micro-pillar compression. *International Journal of Plasticity 105*, 128–140.